machines

MDPI

Article

A Deformation Prediction Method for Thin-Walled Workpiece Machining Based on the Voxel Octree Model

Pengxuan Wei [1], Liping Wang [1,2] and Weitao Li [2,*]

[1] School of Mechanical and Electrical Engineering, University of Electronic Science and Technology of China, Chengdu 611731, China
[2] State Key Laboratory of Tribology in Advanced Equipment, Department of Mechanical Engineering, Tsinghua University, Beijing 100084, China
* Correspondence: liwt@tsinghua.edu.cn

Abstract

In flank milling of thin-walled workpieces, machining deformation is a key issue affecting workpiece accuracy and process stability. Although the traditional finite element method (FEM) offers high accuracy, its low computational efficiency makes it difficult to meet the requirements for rapid prediction in engineering practice. For this purpose, this paper proposes an efficient method for predicting workpiece deformation based on the voxel octree model. First, based on the analysis of the contact position between the cutting tool and the workpiece, the thin-walled workpiece is divided into six levels of voxel units, using a voxel octree model. Then, the stiffness matrix and update model of the voxel units are established. Finally, the deformation prediction is completed by calculating the micro-milling force and the voxel stiffness matrix. The experimental results show that the workpiece deformation predicted by the proposed method is highly consistent with the actual machining measurement. At the same time, compared with traditional FEM and voxel model methods, the calculation time is reduced by 90% and 13.2%, respectively. This method can provide rapid decision support for the optimization of thin-walled workpiece machining processes and effectively improve the efficiency of preliminary research in actual machining.

Keywords: thin-walled workpiece; flank milling; deformation prediction; voxel octree model; milling force

check for updates

Academic Editor: Jun Zha

Received: 22 July 2025
Revised: 26 August 2025
Accepted: 27 August 2025
Published: 3 September 2025

Citation: Wei, P.; Wang, L.; Li, W. A Deformation Prediction Method for Thin-Walled Workpiece Machining Based on the Voxel Octree Model. *Machines* **2025**, *13*, 803. https://doi.org/10.3390/machines13090803

Copyright: © 2025 by the authors. Licensee MDPI, Basel, Switzerland. This article is an open access article distributed under the terms and conditions of the Creative Commons Attribution (CC BY) license (https://creativecommons.org/licenses/by/4.0/).

1. Introduction

Flank milling is widely used in the manufacturing of high-end equipment in industries such as aerospace. Since flank milling involves material removal from the workpiece using a cutting tool, elastic deformation occurs during contact between the tool and the workpiece, leading to machining errors [1,2]. To effectively control such errors, it is essential to predict and compensate for the error through pre-machining simulation. Various methods have been proposed to predict workpiece deformation during flank milling, among which the cantilever beam-based models have been widely adopted and applied [3–5]. However, due to the inherent low stiffness of thin-walled workpieces, they are highly prone to elastic deformation, resulting in significant machining errors. Therefore, conducting research on deformation prediction for thin-walled workpieces is of vital importance.

Existing studies on deformation prediction of thin-walled workpieces are often based on FEM simulation [6–8]. Yan et al. predicted workpiece deformation caused by cutting forces using FEM by constraining the cutting process of thin-walled workpieces [9].

Landwehr et al. optimized the finite element modeling process of workpieces to reduce calculation time, thereby predicting machining deformation by analyzing residual stresses [10]. Peng et al. improved the traditional FEM and proposed an enhanced finite element method for detecting data, which accurately predicts workpiece deformation by forming stress equations [11]. However, in actual milling processes, material removal causes stiffness changes, and the undeformed chips thickness directly affects the calculation of milling forces, making milling forces dependent on the current machining conditions. Therefore, force–deformation coupling must be handled consistently and cannot be replaced by macro-milling forces alone. In existing finite element simulation studies, macro-milling forces are often calculated directly, resulting in errors in the prediction of workpiece deformation. At the same time, although the FEM can effectively predict the deformation of thin-walled workpieces, it requires a large amount of key data to be prepared in advance. Finite element division of the workpiece to be processed involves a large number of matrix calculations, which lead to low prediction efficiency [12–14].

To address this issue, some scholars have proposed methods combining voxel models to improve the efficiency of the thin-walled workpieces deformation prediction. Nishida developed a whole-element model based on cutting edges and instantaneous workpiece deformation, which predicts cutting forces by extracting removed voxel workpiece information to prepare for predicting workpiece deformation [15]. Kaneko proposed a voxel-based milling simulation method that uniformly divides thin-walled workpieces into voxels and then uses discrete voxels and matrix operations to predict workpiece deformation [16]. Wang proposed a method for predicting workpiece deformation by combining FCM and a variable voxel model, which introduces global and local stiffness matrix segmentation techniques to improve computational efficiency [17]. Although these voxel-based methods can effectively improve deformation prediction efficiency, ordinary voxel-based methods often divide thin-walled workpieces into voxels of equal size or coarse voxels for calculation, which increases the amount of calculation at undeformed or slightly deformed parts.

Meanwhile, regenerative chatter and other dynamic issues often accompany the machining of thin-walled workpieces, and we have also conducted relevant research on this problem [18–20]. However, this paper primarily focuses on the foundational step preceding dynamic analysis—quasi-static modeling—which serves as the first step in predicting machining accuracy.

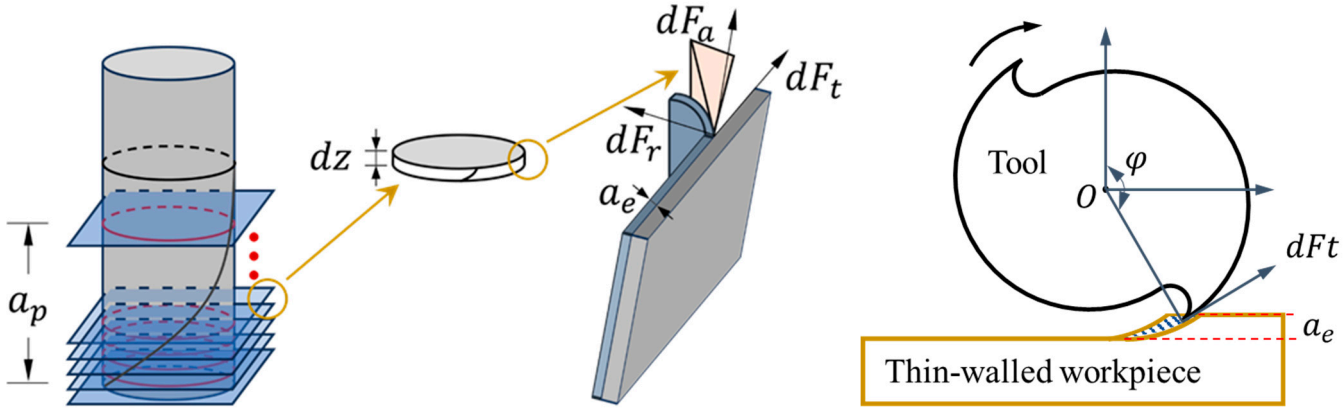
To the end, this study proposes an efficient deformation prediction method for thin-walled workpiece machining based on a voxel octree model, providing a new solution for process optimization. First, a micro-milling force model is established, based on the fundamental assumptions of cutting forces. Then, the contact positions between the tool and the thin-walled workpiece are analyzed, and a six-level voxel adaptive segmentation is performed on the thin-walled workpiece using the octree model method. Additionally, the matrix update and removal methods are optimized. Subsequently, combining the micro-milling force model, the voxel octree model, and the optimized voxel stiffness matrix, the deformation of the workpiece is calculated. Finally, the proposed method is validated through simulation and milling experiments to demonstrate the accuracy and efficiency of predicting thin-walled workpiece deformation during flank milling.

2. Workpiece Deformation Analysis Based on the Voxel Octree Model Method

2.1. Micro-Element Milling Force Model

Based on the proportional relationship between cutting force and instantaneous undeformed chip thickness, this study employs an equivalent shear force model to establish a micro-element milling force model. This modeling method can effectively characterize

the force–thickness relationship during machining, providing accurate mechanical input for subsequent deformation analysis [21]. This model was proposed by Professor Yusuf Altintas and is widely used in the field of mechanical processing. Recent studies have pointed out certain limitations of this method, primarily focusing on the qualitative analysis of stress during plastic deformation, which leads to inaccuracies in the cutting force coefficients [22]. Since the experimental subject of this paper is planar side milling, which does not involve complex surface machining, and the accuracy of the milling force model has already been validated in previous work, this paper selects this milling force model as the foundation for subsequent research [3,23]. Specifically, this model achieves an accurate calculation of cutting forces by discretizing the tool into a series of axially distributed micro-disk elements, as shown in Figure 1. Here, a_p is the cutting depth, a_e is the cutting width, d_z is the thickness of the chip micro-element, and dF_t, dF_r, and dF_a are the tangential, radial, and axial cutting forces of the cutting edge micro-element $\Delta_{i,j}$, respectively.



(**a**) (**b**)

Figure 1. Micro-element milling force model. (**a**) Tool micro-element;(**b**) Cutting diagram.

Based on this modeling method, the equivalent shear force theory is used to establish a micro-element milling force model for the tangential (dF_t), radial (dF_r), and axial (dF_a) cutting force components on each micro-disk element, as shown in Equation (1).

$$\begin{cases} dF_t[\varphi_{i,j}(t)] = [K_{tc} \cdot t_n(i,j,t) + K_{te}] \cdot dz \\ dF_r[\varphi_{i,j}(t)] = [K_{rc} \cdot t_n(i,j,t) + K_{re}] \cdot dz \\ dF_a[\varphi_{i,j}(t)] = [K_{ac} \cdot t_n(i,j,t) + K_{ae}] \cdot dz \end{cases} \tag{1}$$

where $t_n(i,j,t)$ represents the instantaneous undeformed chip thickness at time t for the j-th cutting edge micro-element $\Delta_{i,j}$ on the i-th cutting edge; K_{tc}, K_{rc}, and K_{ac} are the tangential, radial, and axial shear force coefficients related to the undeformed chip thickness t_n, respectively; K_{te}, K_{re}, and K_{ae} are the tangential, radial, and axial cutting edge force coefficients, respectively, and are generally constant terms. These six coefficients will be determined by milling experiments, with units in $\mathrm{N/mm^2}$. d_z is the thickness of the cutting edge micro-element; n_s is the spindle speed. $\varphi_{i,j}(t)$ denotes the position angle of the cutting edge micro-element $\Delta_{i,j}$ on the i-th cutting edge at height z when the tool rotation angle is ωt. The micro-element cutting edge height z can be expressed by Equation (2).

$$z = \frac{2j-1}{2} dz \tag{2}$$

Based on the transformation relationships between the dF_t, dF_r, and dF_a and the axes of the rotational coordinate system, the components of the micro-element cutting force in each axis are expressed by Equation (3).

$$\begin{cases} dF_X^{(r)}(i,j,t) = -\cos\varphi dF_t - \sin\varphi\cos\gamma dF_r + \sin\varphi\sin\gamma dF_a \\ dF_Y^{(r)}(i,j,t) = \sin\varphi dF_t - \cos\varphi\cos\gamma dF_r + \cos\varphi\sin\gamma dF_a \\ dF_Z^{(r)}(i,j,t) = \sin\gamma dF_r + \sin\gamma dF \end{cases} \tag{3}$$

where φ and γ represent the radial and axial position angles of the cutting edge micro-element, respectively, as shown in Equation (4).

$$\begin{cases} \varphi = n_s t + \frac{2(i-1)\pi}{N} + \frac{\pi}{2} - \delta \\ \gamma = 0 \end{cases} \tag{4}$$

where N is the number of cutting edges, i indicates the cutting edge number, and δ is the lag angle of the cutting edge micro-element. Since a flat end mill is used in this paper, γ is 0 degrees.

2.2. The Voxel Octree Model

In finite element static structural analysis, the workpiece is modeled as an elastic solid and discretized into a finite element mesh. Based on the small deformation assumption, this study assumes that the deformation of the workpiece remains within the elastic range and follows Hooke's law. In the FEM model, nodes are classified into two categories: (1) retained nodes located on the machined surface; (2) reduced nodes on the non-machined surface. By concentrating the solution of the displacement field on the retained nodes, it significantly improves computational efficiency while maintaining accuracy.

The octree model is a tree-based data structure based on spatial division. In the octree model, three-dimensional space is represented by a regularly arranged set of cubes, which are recursively divided into several subspaces. Each node represents a three-dimensional region, and each node can have up to eight sub-nodes. Specifically, the octree model divides a cubic space into eight sub-cubes, so that each layer is divided more and more finely until a specific condition (such as maximum depth or minimum spatial scale) is met. Due to this advantage, this paper proposes a method based on the voxel octree model to simulate the deformation of workpieces during milling. In actual simulations, fixed-size voxel models are often chosen to simulate the workpiece, but the size of the voxels can have a certain impact on the milling results, as shown in Figure 2.

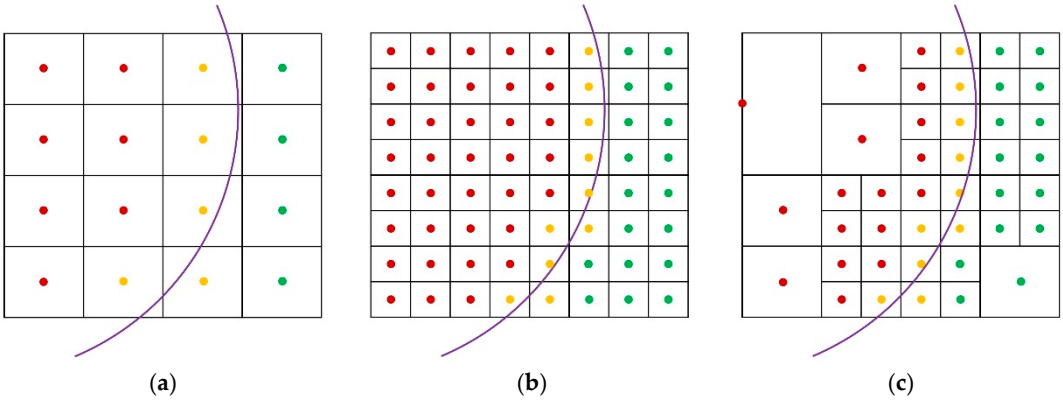


Figure 2. Relationship between the cutting edge and the voxel model. (**a**) Coarse voxel model; (**b**) Fine voxel model; (**c**) Voxel octree model.

As shown in Figure 2, regardless of whether the model is based on coarse or fine voxels, material removal along the tool envelope surface can be effectively achieved during milling. However, in the coarse voxel model (Figure 2a), due to the larger voxel blocks, the cutting edge is farther away from the actual uncut voxel units, which may result in significant errors in stiffness and deformation calculations. In the fine voxel model (Figure 2b), due to the smaller voxel blocks, the cutting edges can be closer to the uncut voxel units, but this greatly increases the computational load of the stiffness model. Therefore, this paper proposes the voxel octree model. It uses large voxel units at locations far from the cutting edge and divides them into smaller voxel units as they become closer to the cutting edge, thereby achieving an efficient and accurate stiffness model and workpiece deformation calculation.

Thin-walled workpieces are typically regarded as elastic bodies, and the radial cutting depth (a_e) during the milling of thin-walled workpieces is generally small. Within the elastic limit of the workpiece, the deformation of the workpiece can be calculated using Hooke's law, based on the milling force and stiffness model. As shown in Figure 2c, in the voxel octree model, octree nodes can be further divided into three types: red completely removed nodes (CR), yellow cutting edge micro-element nodes (ER), and green unremoved nodes (UR). In order to solve the accurate deformation of thin-walled workpieces based on the voxel octree model, this paper further studies the construction and updating of the stiffness matrix.

Since the unit size of the voxel octree model directly affects the accuracy and efficiency of workpiece deformation calculations, selecting the appropriate octree depth is essential. According to the computational complexity of the octree model ($nlogn$), it can be seen that the number of units increases to $n * 8$ for each additional level of depth, resulting in a tenfold increase in computational complexity [24]. Based on the size of the thin-walled workpiece and the axial difference in the micro-element milling force in this paper, it can be calculated that the octree depth should be selected between five and seven. The accuracy of the five-level octree model is relatively low, and the computational complexity of the seven-level octree model increases tenfold. Therefore, this paper chooses the octree model with a depth of six.

2.3. Stiffness Matrix Construction and Update Method

Each voxel octree node is connected to adjacent octree nodes using the same beam elements as in traditional FEM, as shown in Figure 3. The center points $O1$ and $O2$ of adjacent voxel octree models correspond to eight vertices, but in the actual voxel calculation process, the two center points correspond to twelve vertices, as shown in Figure 4.

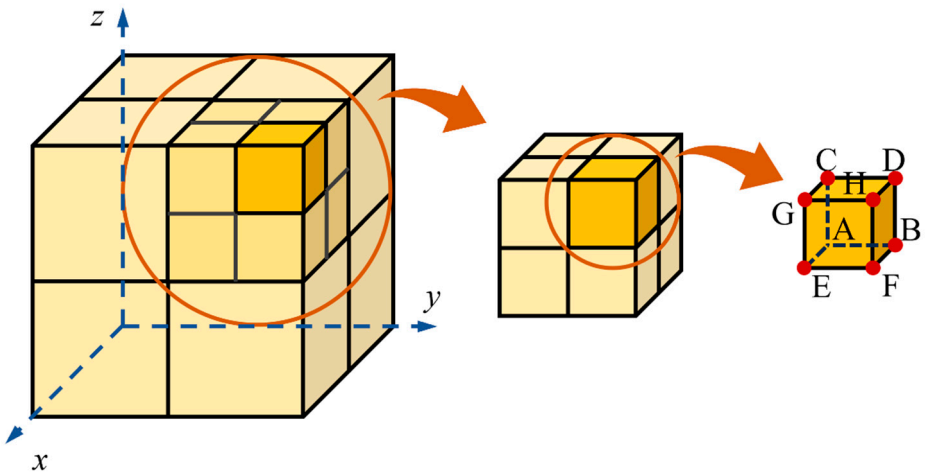


Figure 3. Vertex subdivision of the voxel octree model.

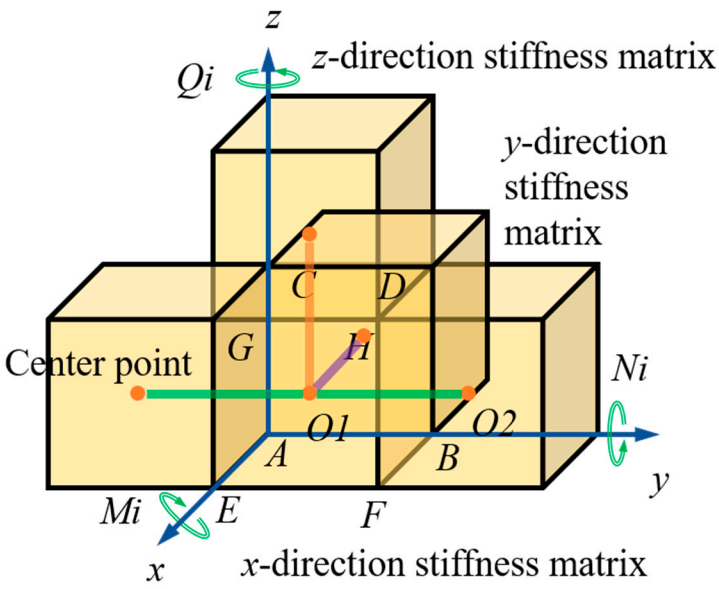


Figure 4. Adjacent voxels and deflection relationships.

As shown in Figure 4, the center points of the voxels and the corresponding nodes are regularly distributed in the *x*-*y*-*z* directions. Therefore, only three types of unit matrix need to be considered, which are the *x*-direction stiffness matrix K_{ex}, the *y*-direction stiffness matrix K_{ey}, and the *z*-direction stiffness matrix K_{ez}. K_{ex} links two adjacent voxel units in the x-direction. For voxel units in the *y* and *z* directions, the K_{ey} and K_{ez} are obtained by applying a rotation matrix to K_{ex}. Then, the stiffness matrix K of the entire workpiece is calculated based on the voxel connectivity and the three stiffness matrixes K_{ex}, K_{ey}, and K_{ez}. Assuming that the force vector between octree voxel units is F_e, the relationship between K_{ex} and the displacement vector is given by Equation (5).

$$F_e = K_{ex} \cdot d_e \tag{5}$$

Each node has six degrees of freedom, consisting of three translational and three rotational degrees of freedom. Therefore, the corresponding vectors F_e, d_e, and K_{ex} can be expressed by Equations (6)–(8).

$$F_e = \begin{bmatrix} F_{xi} & F_{yi} & F_{zi} & M_i & N_i & Q_i & F_{xj} & F_{yj} & F_{zj} & M_j & N_j & Q_j \end{bmatrix}^T \tag{6}$$

$$d_e = \begin{bmatrix} x_i & y_i & z_i & \alpha_i & \beta_i & \gamma_i & x_j & y_j & z_j & \alpha_j & \beta_j & \gamma_j \end{bmatrix} \tag{7}$$

$$K_{ex} = \begin{bmatrix} K_{11} & K_{12} \\ K_{21} & K_{22} \end{bmatrix} \tag{8}$$

Substituting the moments of inertia I_x, I_y, I_z and section modulus J of the aluminum alloy thin-walled workpiece into the stiffness matrix K_{ij}, Equation (9) can be obtained.

$$K_{ij} = \begin{bmatrix} K_{xx} & K_{xy} & K_{xz} & K_{x\theta_x} & K_{x\theta_y} & K_{x\theta_z} \\ K_{yx} & K_{yy} & K_{yz} & K_{y\theta_x} & K_{y\theta_y} & K_{y\theta_z} \\ K_{zx} & K_{zy} & K_{zz} & K_{z\theta_x} & K_{z\theta_y} & K_{z\theta_z} \\ K_{\theta_x x} & K_{\theta_x y} & K_{\theta_x z} & K_{\theta_x \theta_x} & K_{\theta_x \theta_y} & K_{\theta_x \theta_z} \\ K_{\theta_y x} & K_{\theta_y y} & K_{\theta_y z} & K_{\theta_y \theta_x} & K_{\theta_y \theta_y} & K_{\theta_y \theta_z} \\ K_{\theta_z x} & K_{\theta_z y} & K_{\theta_z z} & K_{\theta_z \theta_x} & K_{\theta_z \theta_y} & K_{\theta_z \theta_z} \end{bmatrix} \tag{9}$$

The bending stiffness (y-z plane) is expressed by Equations (10) and (11).

$$K_{yy} = K_{zz} = \frac{12EI}{L^3} \tag{10}$$

$$K_{y\theta_y} = K_{z\theta_z} = \frac{6EI}{L^2} \tag{11}$$

The shear stiffness (x plane) is expressed by Equation (12).

$$K_{xx} = \frac{EA}{L} \tag{12}$$

The torsional stiffness is expressed by Equation (13).

$$K_{\theta_x\theta_x} = \frac{GJ}{L} \tag{13}$$

By combining the above equations, four stiffness matrixes, K_{11}, K_{12}, K_{21}, and K_{22}, can be obtained. Specifically, as shown in Equations (14)–(17):

$$K_{11} = \begin{bmatrix} \frac{EA}{L} & 0 & 0 & 0 & 0 & 0 \\ 0 & \frac{12EI}{L^3} & 0 & 0 & 0 & \frac{6EI}{L^2} \\ 0 & 0 & \frac{12EI}{L^3} & 0 & -\frac{6EI}{L^2} & 0 \\ 0 & 0 & 0 & \frac{GJ}{L} & 0 & 0 \\ 0 & 0 & -\frac{6EI}{L^2} & 0 & \frac{4EI}{L} & 0 \\ 0 & \frac{6EI}{L^2} & 0 & 0 & 0 & \frac{4EI}{L} \end{bmatrix} \tag{14}$$

$$K_{12} = \begin{bmatrix} -\frac{EA}{L} & 0 & 0 & 0 & 0 & 0 \\ 0 & -\frac{12EI}{L^3} & 0 & 0 & 0 & \frac{6EI}{L^2} \\ 0 & 0 & \frac{12EI}{L^3} & 0 & -\frac{6EI}{L^2} & 0 \\ 0 & 0 & 0 & -\frac{GJ}{L} & 0 & 0 \\ 0 & 0 & -\frac{6EI}{L^2} & 0 & \frac{2EI}{L} & 0 \\ 0 & \frac{6EI}{L^2} & 0 & 0 & 0 & \frac{2EI}{L} \end{bmatrix} \tag{15}$$

$$K_{21} = K_{12}^T \tag{16}$$

$$K_{22} = \begin{bmatrix} \frac{EA}{L} & 0 & 0 & 0 & 0 & 0 \\ 0 & \frac{12EI}{L^3} & 0 & 0 & 0 & -\frac{6EI}{L^2} \\ 0 & 0 & \frac{12EI}{L^3} & 0 & \frac{6EI}{L^2} & 0 \\ 0 & 0 & 0 & -\frac{GJ}{L} & 0 & 0 \\ 0 & 0 & \frac{6EI}{L^2} & 0 & \frac{2EI}{L} & 0 \\ 0 & -\frac{6EI}{L^2} & 0 & 0 & 0 & \frac{2EI}{L} \end{bmatrix} \tag{17}$$

where A is the area of the cross section; E is Young's modulus; G is the shear modulus; I_y and I_z are the moments of inertia of the cross section; and J is the torsional constant of the cross section.

The shear modulus G can be calculated with Young's modulus E and the Poisson's ratio ν, as shown in Equation (18). The moments of inertia I and the torsional constant J are calculated with Equations (19) and (20).

$$G = \frac{E}{2(1+v)} \tag{18}$$

$$I = \frac{L^4}{12} \tag{19}$$

$$J = \frac{L^4}{6} \tag{20}$$

In the milling process, the shape of thin-walled workpieces constantly changes, causing the stiffness matrix of the workpiece to be continuously updated. Using traditional FEM to update the stiffness matrix requires frequent mesh division based on the shape of the workpiece, which reduces the efficiency of the calculation. This paper updates the stiffness matrix by removing voxel units based on the voxel octree model method. This method avoids redividing the finite element mesh of the workpiece, making the stiffness matrix update simpler and more efficient.

$$K_{i+1} = K_{i-1} - K_r \tag{21}$$

The stiffness matrix update method used in this paper is shown in Figure 5. As mentioned above, when the tool collides with the voxel octree node, the node is removed, and the stiffness matrix of the node is also removed. Assume that the stiffness matrix of the voxel octree model is K_{i-1}, and the upper right voxel is cut off. Then, the stiffness matrix K_r of this node must be removed from the original model stiffness matrix. Finally, the updated stiffness matrix is obtained, as shown in Equation (21).

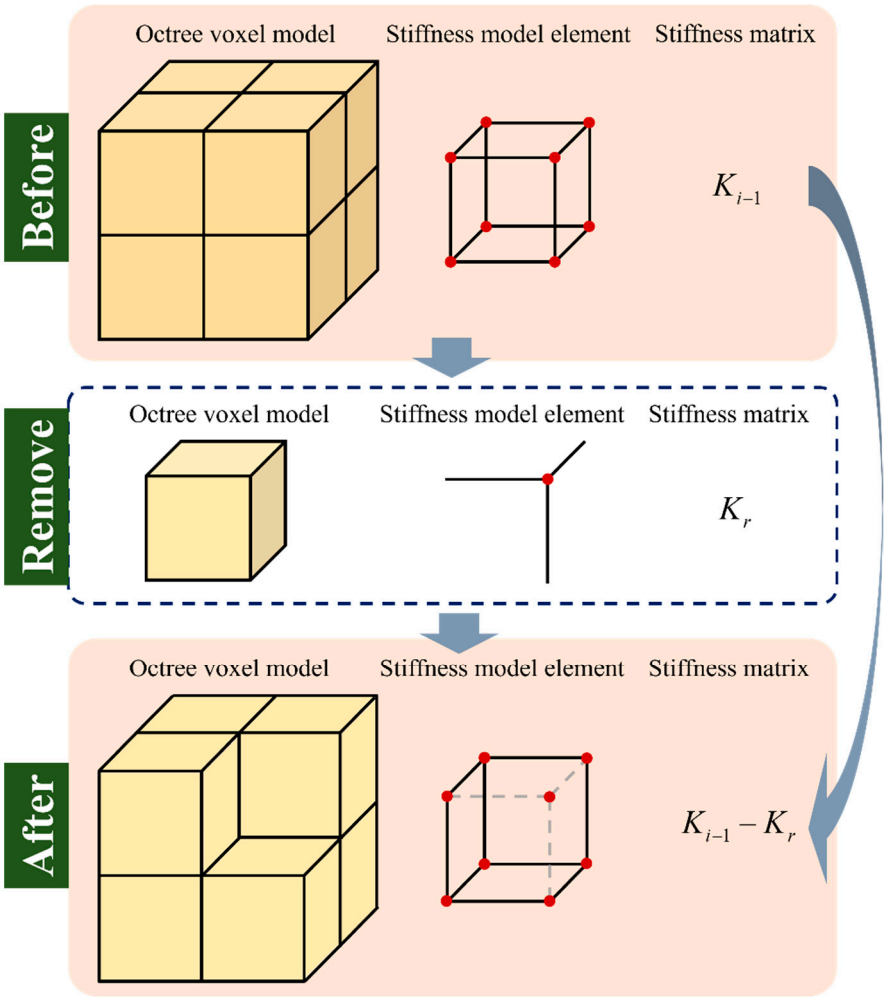


Figure 5. Matrix update method.

2.4. Rapid Calculation of Workpiece Deformation

According to the voxel unit distribution of the proposed voxel octree model, the octree depth is six. Then, the voxel units of the voxel octree can be divided into six levels,

namely, overall units (level 1), coarse voxel units (levels 2 and 3), and fine voxel units (levels 4, 5, and 6). The deformation amount of the workpiece can be calculated in two steps, which are the initial deformation calculation and the accurate deformation calculation. Specifically, the flowchart for calculating the deformation of thin-walled workpieces based on the voxel octree model method is shown in Figure 6.

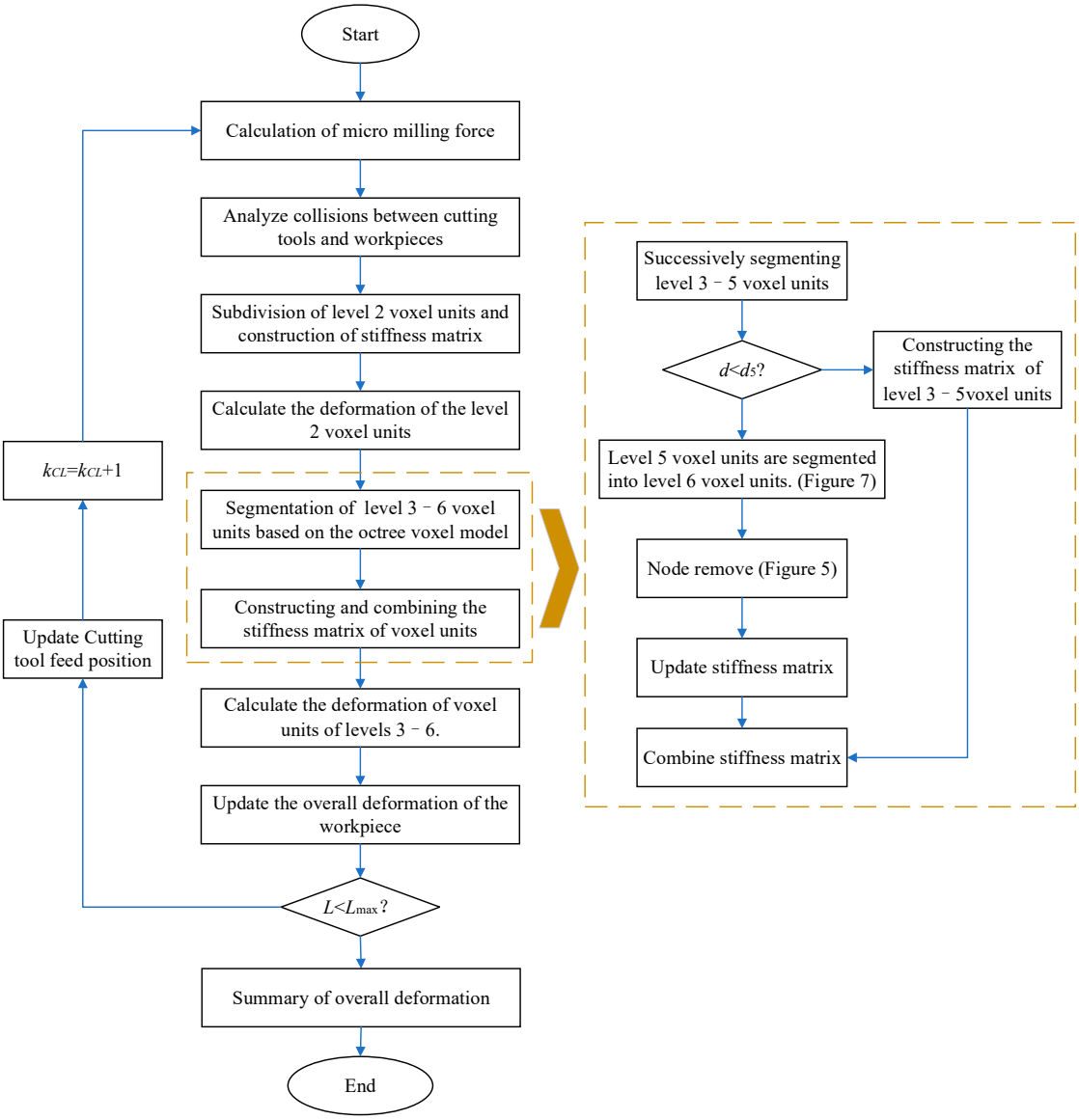


Figure 6. Flowchart of workpiece deformation calculation.

As shown in Figure 6, first calculate the micro-element milling force and analyze the collision between the milling cutter and the workpiece. Divide the workpieces into level 2 voxel units and calculate the deformation. Since the unit grid of the level 2 voxel units is relatively sparse, the initial deformation of the workpiece can be calculated more quickly. This step can quickly approximate the actual deformation of the workpiece and effectively reduce the complexity of the calculation efficiency. Then, voxel units at appropriate positions are divided according to the voxel octree model. Stiffness matrixes corresponding to level 3–6 voxel units are constructed, and deformation is calculated in combination with microelement milling force. Finally, the deformation of level 2, 3, 4, and 5 voxel units is uniformly subdivided into level 6 voxel units, and the overall deformation of the workpiece is obtained by summarizing them.

The appropriate location for voxel unit segmentation needs to be discussed on a case-by-case basis. The segmentation strategy for level 2 to 5 voxel units is different, and the specific rules are as follows. As defined by the voxel octree model, the next level of voxel units can be obtained by dividing the previous level of voxel units using the octree method. First, the level 1 voxel units of the workpiece are divided into level 2 voxel units. When a voxel unit contains a cutting edge, the level 2 voxel units are divided into level 3 voxel units using the octree theory. The voxel elements are further traversed. If the level 3 voxel unit does not contain any cutting edges, retain this level. Otherwise, continue to divide the level 3 voxel unit into level 4 voxel units through octree theory. Continuing from the previous step, divide the level 4 voxel units by determining whether the unit contains a cutting edge. The division rules for level 5 voxel units are determined by the distance from the center point of the unit to the cutting edge, as shown in Figure 7. When the distance d between the center point of the level 5 voxel unit and the cutting edge is less than the center point spacing d_5 of the voxel unit, the level 5 voxel unit is further divided into level 6 voxel units according to the octree theory. Furthermore, a sensitivity analysis was performed on parameter d, as shown in Table 1. $0.8d_5$ lead to a decrease in the number of voxel units but improved computational efficiency; $1.2d_5$ lead to an increase in the number of voxel units but reduced computational efficiency. Through comprehensive analysis, it was found that only at one time, d_5, can both efficiency and accuracy be balanced. Therefore, when the distance d between the cutting edge and the center point of the level 5 voxel unit is less than d_5, octree segmentation should continue. As can be seen in Figure 7, the green dotted line indicates that the distance d between the center point of the level 5 voxel unit and the cutting edge does not meet the octree division condition, so the original voxel unit is retained. The red dotted line indicates that the distance d meets the division condition, so the level 5 voxel unit is further divided into level 6 voxel units through octree theory.

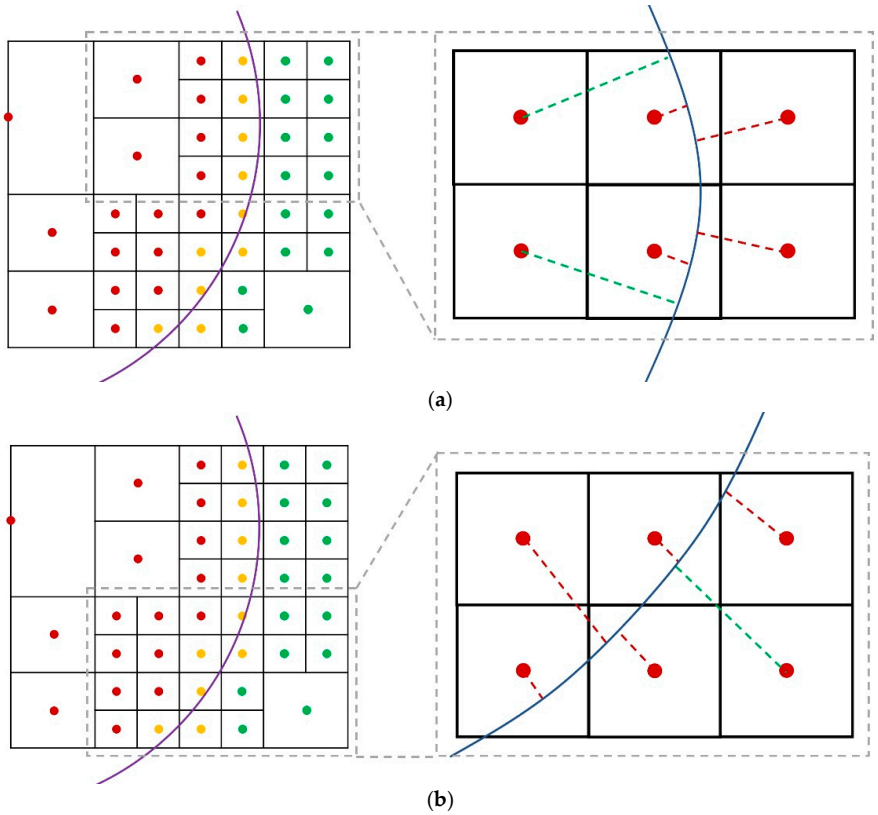


Figure 7. Segmentation rules of level 5 voxel unit octree. (**a**) Upper half of a level 5 voxel unit; (**b**) Lower half of a level 5 voxel unit.

Table 1. Sensitivity analysis of distance d.

Distance Judgment (d<x)	Number of Voxel Units	Computational Time (ms)
1*d_5	1684	523
0.8*d_5	1428	392
1.2*d_5	1940	715

After modeling thin-walled workpieces with the voxel octree model, the stiffness matrix of each level of voxel units needs to be divided. According to the division rules, the stiffness matrices in the X and Y directions of the previous level voxel units are divided into four submatrices, as shown in Equation (22).

$$K_{\mathrm{Xup}} = \begin{bmatrix} K_{\mathrm{Xnext1}} & K_{\mathrm{Xnext2}} \\ K_{\mathrm{Xnext3}} & K_{\mathrm{Xnext4}} \end{bmatrix} \tag{22}$$

where K_{Xup} is the stiffness matrix of the x-direction of the previous level voxel unit; K_{Xnext1}–K_{Xnext4} are the sub-stiffness matrices of the x-direction of the next level voxel unit. The sub-stiffness matrices in the Y and Z directions are obtained by rotating and splitting K_{Xup}. The rotation matrix of K_{Xup} to K_{Yup} is R_z, and the rotation matrix of K_{Xup} to K_{Zup} is R_y, which are expressed in Equations (23) and (24).

$$R_z = \begin{bmatrix} 0 & -1 & 0 \\ 1 & 0 & 0 \\ 0 & 0 & 1 \end{bmatrix} \tag{23}$$

$$R_y = \begin{bmatrix} 0 & 0 & 1 \\ 0 & 1 & 0 \\ -1 & 0 & 0 \end{bmatrix} \tag{24}$$

From the rotation matrices R_z and R_y, K_{Yup} and K_{Zup} can be obtained, as shown in Equations (25) and (26).

$$K_{Yup} = R_z K_{Xup} R_z^T \tag{25}$$

$$K_{Zup} = R_y K_{Xup} R_y^T \tag{26}$$

Since the octree segmentation method involves multiple levels of voxel units, the stiffness matrices of each voxel unit are not consistent. This paper ensures the continuity of the stiffness matrix by sharing nodes. Specifically, the stiffness contribution of shared nodes is obtained by weighted summation, as shown in Equation (27).

$$K_{share} = w_1 \cdot K_{s1} + w_2 \cdot K_{s2} + \cdots + w_n \cdot K_{sn} \tag{27}$$

where K_{share} is the composite stiffness matrix of the shared node; K_{s1}, K_{s2}, ..., and K_{sn} are the stiffness matrices of the n individual voxel units connected to this node; w_i is the weight coefficient of the i-th individual voxel unit, which is determined by the proportion of the voxel volume. When a voxel unit is removed, its volume becomes 0, and it is automatically removed from Equation (27).

As described above, once the micro-element milling forces and the stiffness matrix splitting rules for each level of voxel units are determined, the deformation of thin-walled workpieces can be further calculated. First, the deformation of the level 1 voxel unit is calculated, as shown in Equation (28). The deformation of the subsequent voxel units is calculated according to Equation (29), and the solution is continued until the deformation of the level 6 voxel unit is obtained. Since this paper selects side milling of thin-walled

workpieces, the proportion of the main cutting force is much greater than that of the lateral cutting force, which reduces the risk of plastic deformation caused by bending moment. Therefore, this paper simplifies the workpiece deformation to elastic deformation for analysis. Finally, the complete deformation of the thin-walled workpiece is obtained by combining the deformation amounts using Equation (30).

$$d_1 = \frac{F_1}{K_1} \tag{28}$$

$$\begin{bmatrix} K_{i+1_1} & K_{i+1_2} & K_{i+1_3} & K_{i+1_4} \end{bmatrix} \begin{bmatrix} d_{i+1_1} \\ d_{i+1_2} \\ d_{i+1_3} \\ d_{i+1_4} \end{bmatrix} = \begin{bmatrix} F_{i+1_1} & F_{i+1_2} & F_{i+1_3} & F_{i+1_4} \end{bmatrix} \tag{29}$$

$$d_{whole} = \begin{bmatrix} d_1 & \dots & d_1 & d_1 & d_1 & d_1 & d_2 & d_2 & d_2 & d_2 & \dots & d_1 \\ \vdots & \ddots & \vdots & \vdots & \vdots & \vdots & \vdots & \vdots & \vdots & \vdots & \iddots & \vdots \\ d_1 & \dots & d_4 & d_4 & d_5 & d_5 & d_6 & d_6 & d_6 & d_6 & \dots & d_1 \\ d_1 & \dots & d_4 & d_4 & d_5 & d_5 & d_6 & d_6 & d_6 & d_6 & \dots & d_1 \\ d_1 & \dots & d_4 & d_4 & d_5 & d_5 & d_6 & d_6 & d_6 & d_6 & \dots & d_1 \\ d_1 & \dots & d_4 & d_4 & d_5 & d_5 & d_6 & d_6 & d_6 & d_6 & \dots & d_1 \\ d_1 & \dots & d_5 & d_5 & d_6 & d_6 & d_6 & d_6 & d_6 & d_6 & \dots & d_1 \\ d_1 & \dots & d_5 & d_5 & d_6 & d_6 & d_6 & d_6 & d_6 & d_6 & \dots & d_1 \\ d_1 & \dots & d_5 & d_5 & d_6 & d_6 & d_6 & d_6 & d_5 & d_5 & \dots & d_1 \\ d_1 & \dots & d_5 & d_5 & d_6 & d_6 & d_6 & d_6 & d_5 & d_5 & \dots & d_1 \\ \vdots & \iddots & \vdots & \vdots & \vdots & \vdots & \vdots & \vdots & \vdots & \vdots & \ddots & \vdots \\ d_1 & \dots & d_2 & d_2 & d_2 & d_2 & d_1 & d_1 & d_1 & d_1 & \dots & d_1 \end{bmatrix} \tag{30}$$

where F_1 and K_1 are the milling force and stiffness matrix corresponding to the level 1 voxel unit; K_{i+1_1} to K_{i+1_4} are the stiffness matrix of the next level voxel unit; d_{i+1_1} to d_{i+1_4} are the deformation amount of the next level voxel unit; and F_{i+1_1} to F_{i+1_4} are the milling force corresponding to the next level voxel unit. d_{whole} is the overall deformation amount, and d_1 to d_6 are the deformation amounts of each level voxel units, respectively.

Based on the proposed stiffness matrix update method, the local heat map of the thin-walled workpiece stiffness can be further obtained, as shown in Figure 8. It can be seen that the bottom of the workpiece is fixedly constrained, so the stiffness is maximum, and along the positive z-axis direction, the stiffness gradually decreases. After side milling, due to material removal, the stiffness matrix of the voxel element is removed, and the stiffness matrix is also updated accordingly.

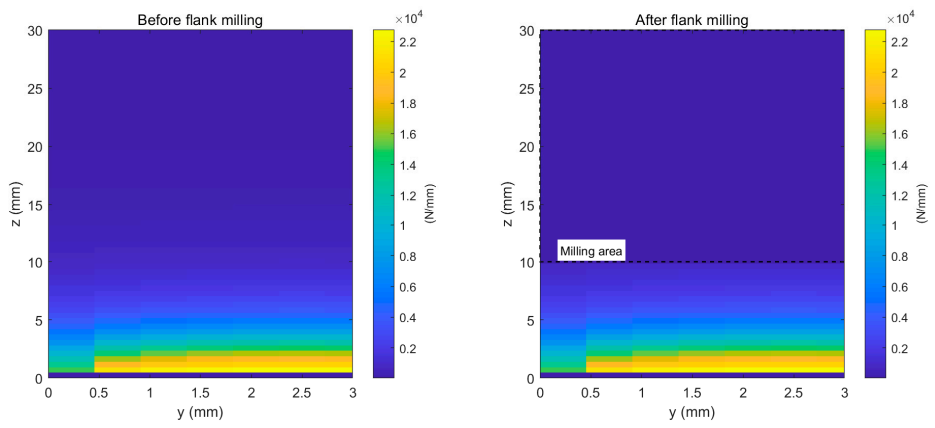


Figure 8. Local heat map of thin-walled workpiece stiffness.

3. Workpiece Deformation Simulation

In this paper, a 2.4 mm thin-walled workpiece made of 7075 aluminum alloy and a Φ16 mm flat-end milling cutter were selected for flank milling simulation experiments. The specific experimental parameters are shown in Table 2, where the milling depth is 20 mm, the milling width is 0.4 mm, the spindle speed is 6000 r/min, and the feed rate is 1800 mm/min. Since the calculation of machining deformation requires milling force simulation, the specific simulation parameters are shown in Table 3. The six cutting force coefficients in Table 3 were obtained by eight sets of flank milling orthogonal experiments on thin-walled workpieces [21,23,25,26]. In order to facilitate the deformation solution, the thin-walled workpiece is regarded as a cantilever beam model: that is, the bottom of the thin-walled workpiece is treated as a fixed end.

Table 2. Processing experiment parameters.

Thin-walled workpiece parameters	Length (mm)	200
	Width (mm)	2.4
	Heigh (mm)	30
Tool parameters	Diameter (mm)	16
	Length (mm)	120
	Helix angle (°)	25
	Material	H10F
	Number of teeth	2
	Radial rake angle (°)	17
	Axial rake angle (°)	1
	Normal rake angle (°)	8.3
	Edge inclination angle (°)	65
Processing parameters	Milling depth (mm)	20
	Milling width (mm)	0.4
	Spindle speed (r/min)	6000
	Feed rate (mm/min)	1800

Table 3. Model simulation parameters.

Levels of the voxel octree model	6	
Workpiece material parameters	Young's modulus (GPa)	6.9
	Poisson coefficient	0.25
Tool material parameters	Flexural strength (N/mm^2)	4300
	Young's modulus (GPa)	5.2
Cutting force coefficient	K_{ae} (N/mm)	0.83
	K_{re} (N/mm)	16.07
	K_{te} (N/mm)	7.59
	K_{ac} (N/mm^2)	82.51
	K_{rc} (N/mm^2)	321.49
	K_{tc} (N/mm^2)	1173.41

According to the simulation conditions, the flank milling process was simulated, as shown in Figure 9. The red color represents the flat-end milling cutter model, and the green color represents the thin-walled aluminum alloy workpiece. It can be seen that the thin-walled workpiece is divided into six levels of voxel models according to the octree theory. The voxel units far away from the tool are divided into low-level voxel units, and the closer to the tool, the higher the level of the voxel units.

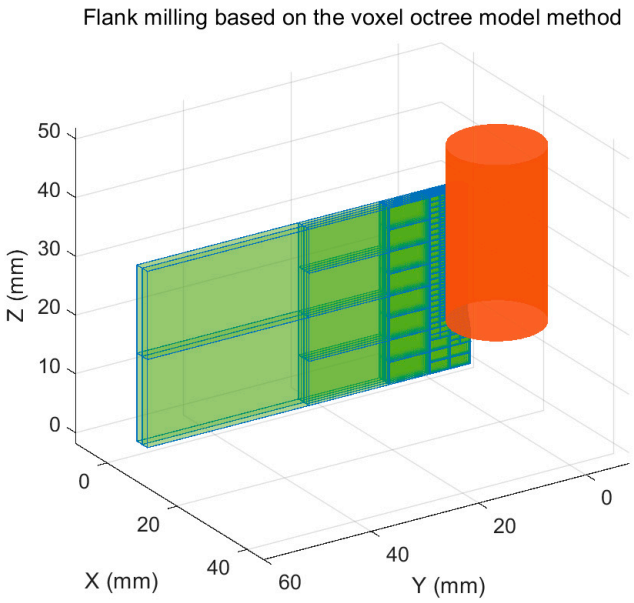


Figure 9. Simulation of flank milling based on the voxel octree model method.

In actual machining, flank milling deformation of thin-walled workpieces mainly occurs in the radial direction of the tool. Therefore, this paper mainly investigates the deformation of the flank milling end of the workpiece, i.e., the deformation in the x-direction. The milling force in the *x*-direction is obtained according to the simulation parameters in Table 2, as shown in Figure 10. As can be seen from the figure, the peak milling force information for tooth 1 and tooth 2 is shown. Since the two-tooth milling tool used in this paper has uneven tooth load issues, there is a difference in the peak milling force between the two teeth [27].

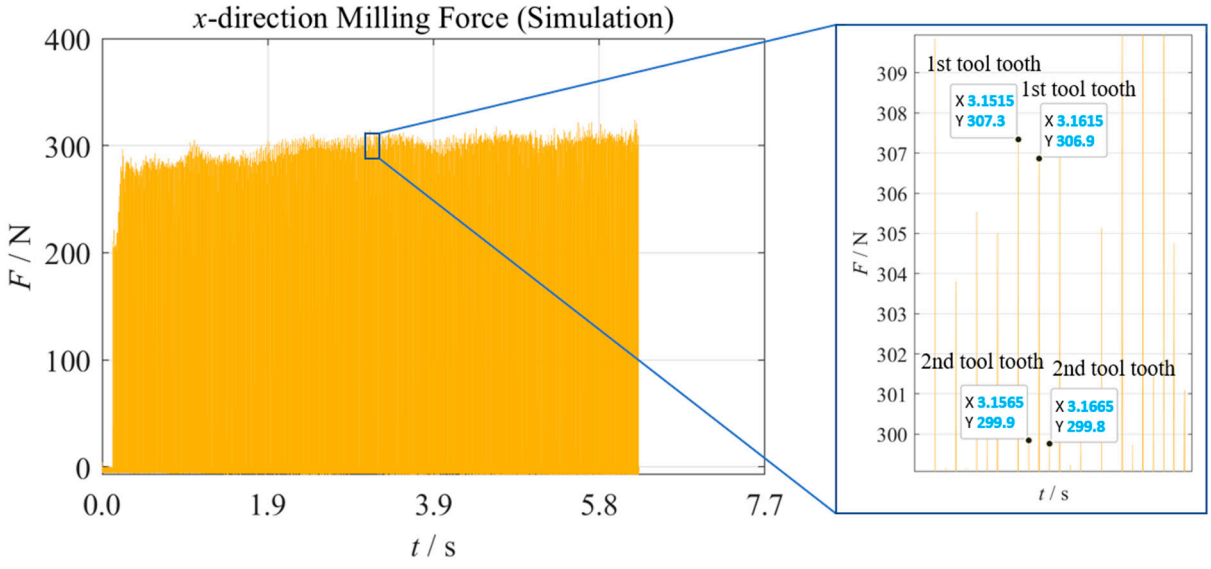


Figure 10. Simulation of milling force in the *x*-direction.

The overall deformation of the aluminum alloy thin-walled workpiece in the x-direction was calculated using the voxel octree model proposed in this paper, as shown in Figure 11. It can be seen that the overall deformation of the workpiece is not uniform. Along the y-direction, the deformation at the edges of the workpiece is significantly greater than that at the center, which is due to the weaker stiffness of the edges compared to the

center. Along the z-direction, the deformation at the bottom is smaller, which is caused by considering the workpiece to be a cantilever beam model.



Figure 11. Simulation results of overall deformation of thin-walled workpiece.

4. Processing Experiment Results and Discussion

In order to further investigate the effectiveness of the voxel octree method in predicting workpiece deformation during actual flank milling, this paper selected the SMC125u five-axis hybrid machine tool to perform milling experiments on thin-walled aluminum alloy workpieces, as shown in Figure 12. To avoid randomness in a single experiment, a total of 10 thin walls were milled in this experiment, and the measurement results were averaged.

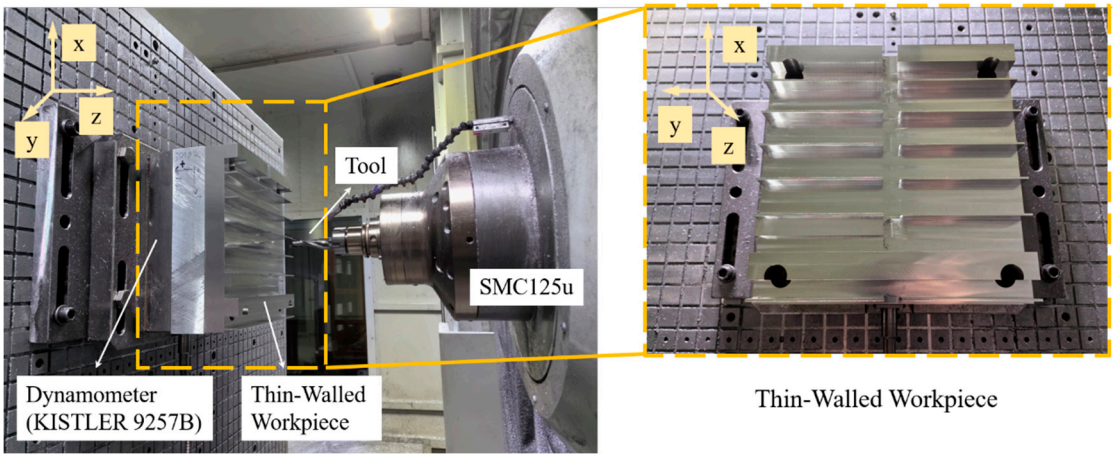


Figure 12. Flank milling experiment on thin-walled workpieces.

During the machining process, the KISTLER 9255C dynamometer was used to simultaneously measure the x-direction milling force, and the milling force results shown in Figure 13 were obtained. The dynamometer settings are as follows: the sampling frequency is 4000, the filter type is a low-pass filter, and the average force calculation is the period average. The simulation results and experimental results of the x-direction milling force are shown in Figure 14. Since the cutting coefficients provided in Table 3 were calibrated in advance using the same machining method as the machining experiment, and Figure 14 shows that the amplitude of the simulated milling force and the experimental milling force

are basically consistent, it can be concluded that the milling force model in this paper is correct.

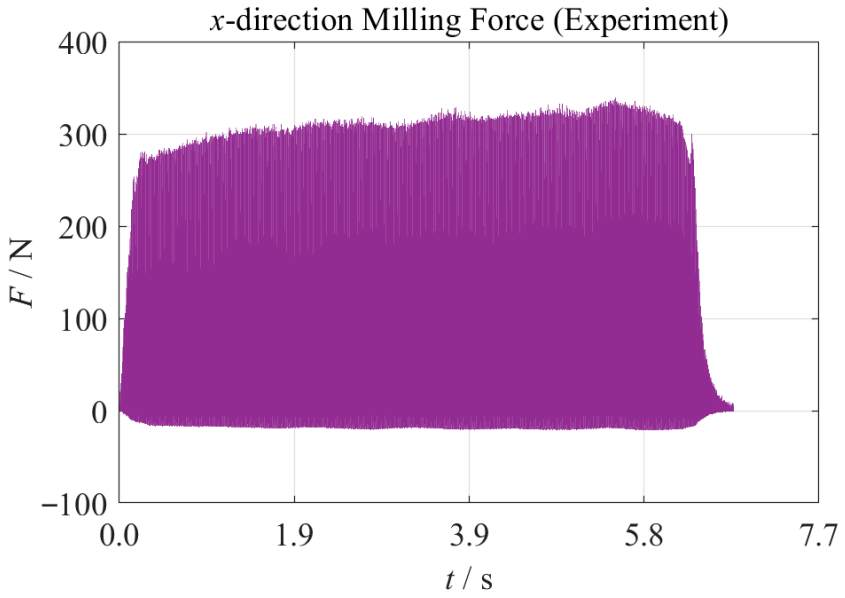


Figure 13. *x*-direction milling force measured during processing experiment.

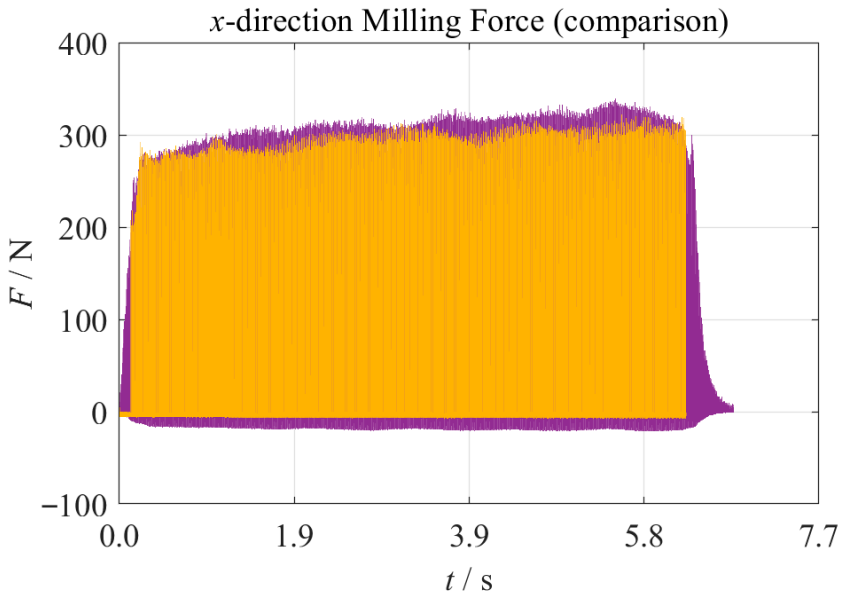


Figure 14. Comparison of simulated and actual measured values of *x*-direction milling force.

The thickness of the thin-walled workpiece is obtained by measuring the machined thin-walled workpiece with a coordinate measuring machine (CMM), and the amount of deformation can be further calculated, as shown in Figure 15. This CMM is Hexagon's EXPLORER 07.10.07, which uses a standard ball to calibrate the touch-trigger probe. The CMM's uncertainty is 3 μm. The CMM measured 10 points along the *y*-direction and 5 points along the *z*-direction of the thin-walled workpiece, as shown in Figure 16. The measurement results of the thin-walled workpiece deformation along the *y*-direction are shown in Figure 17a, and those along the *z*-direction are shown in Figure 17b. It can be seen that along the *y*-direction, the actual measured deformation of thin-walled workpieces decreases and then increases; along the *z*-direction, the actual measured deformation of thin-walled workpieces increases and then decreases, which is consistent with the trend of the simulated deformation of thin-walled workpieces.

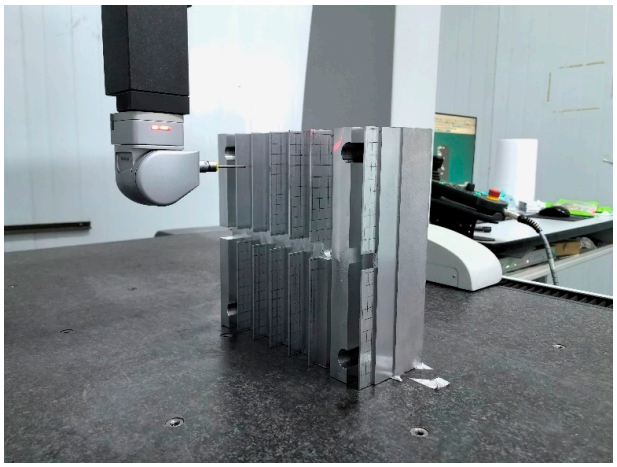


Figure 15. Measurement of the thin-walled workpiece.

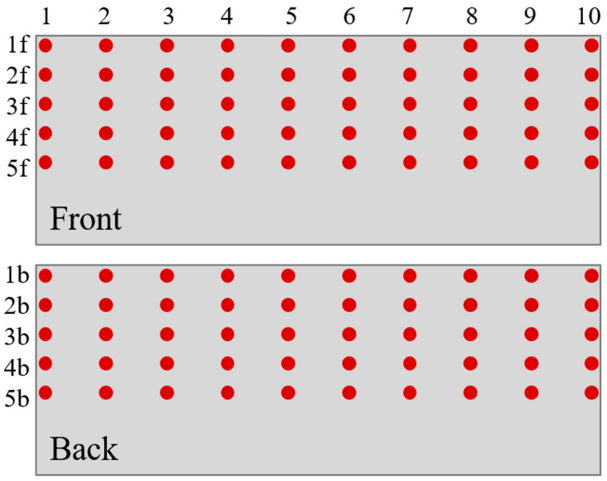


Figure 16. Distribution of measurement points.

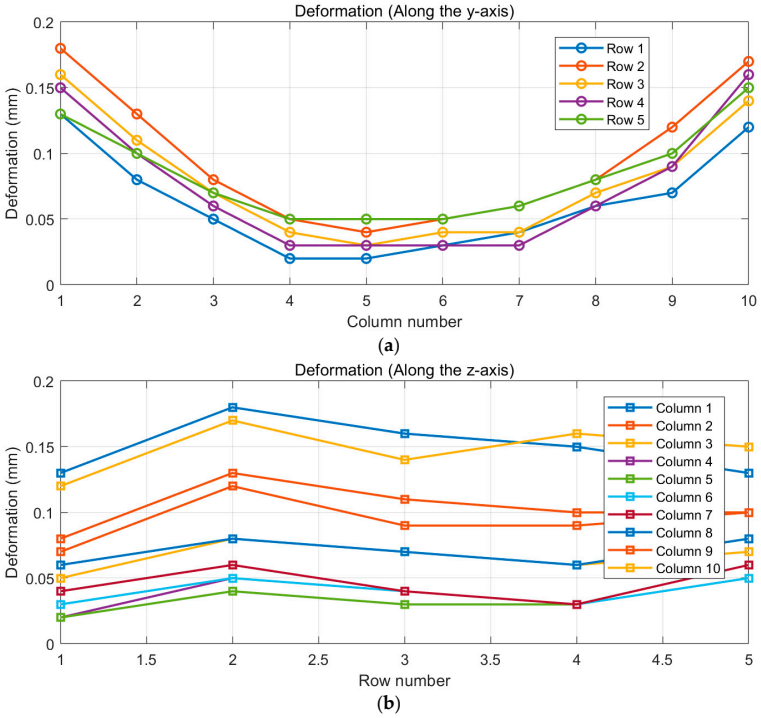


Figure 17. Actual measured deformation values. (**a**) Arranged along the *y*-axis; (**b**) Arranged along the *z*-axis.

Furthermore, the deformation results of the simulation and actual measured values in Row 3 and Column 4 were randomly selected for comparison, as shown in Figure 18. As shown in the figure, the maximum deformation difference in Row 3 is 0.02 mm, and the minimum deformation difference is 0 mm; the maximum deformation difference in Column 4 is 0.02 mm, and the minimum deformation difference is 0 mm. Regardless of whether the deformation in the simulation and the actual measured deformation differs by less than 0.02 mm, it can be proven that the voxel octree model proposed in this paper for predicting deformation is accurate.

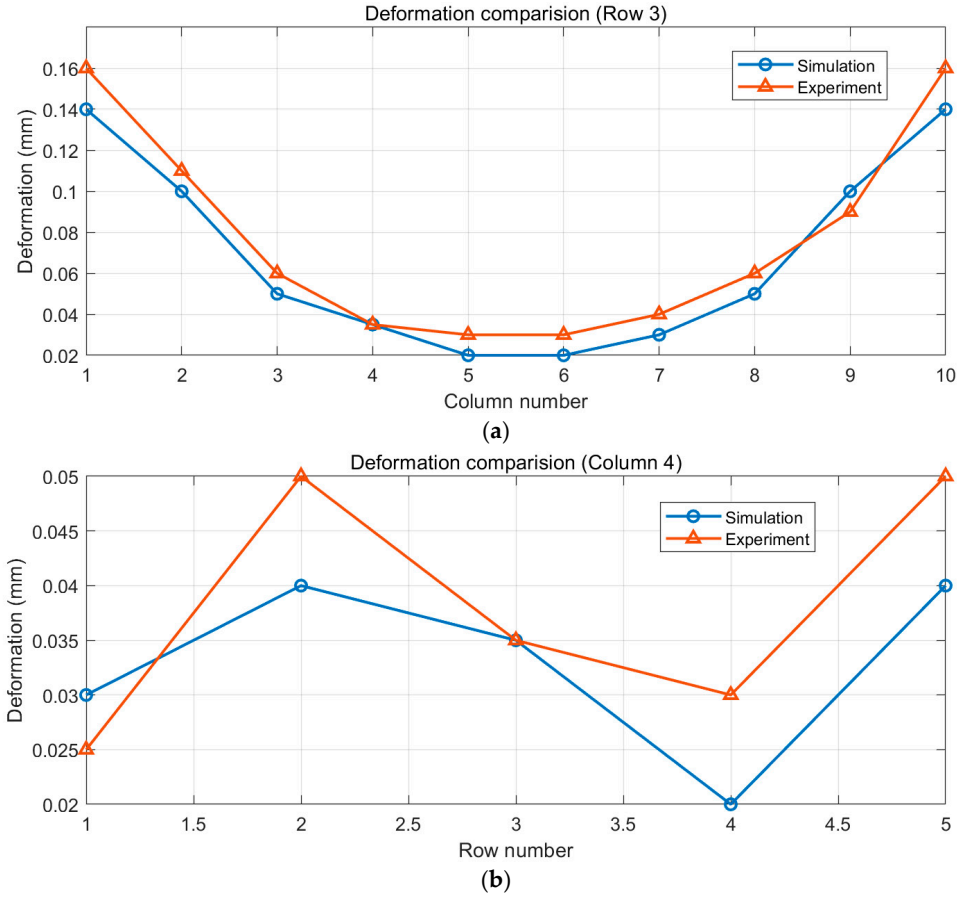


Figure 18. Comparison of simulated and measured values of workpiece deformation for random matrices. (**a**) Comparison results for Row 3; (**b**) Comparison results for Column 4.

Meanwhile, this paper compares the efficiency of deformation prediction using traditional FEM, the voxel model method [16], and the voxel octree model method, with the results shown in Table 4 and Figure 19. The hardware configuration of the computational platform is Windows 11 with an Intel Core i7-13700 processor. The simulation software based on FEM is Workbench 23 R1. The tool is treated as the rigid body, and the bottom of the workpiece is fixedly connected. The element type is a quadratic element, the mesh size is 0.2 mm, the material removal is element erosion, the time step is 1.5×10^{-7}, the displacement residual is 0.5%, and the stopping criterion is tool displacement of 200 mm. As shown in the table and the figure, the voxel octree model method demonstrates significant improvements compared to the other two methods, achieving more than a 90% increase compared to the traditional FEM and a 13.2% increase compared to the voxel segmentation method. Specifically, the computational complexity of the three methods is compared in Table 5, where n represents the number of cells/voxels, n_c and n_f represent the number of coarse and fine voxels, respectively. It can be seen that the computational complexity (memory occupation, single step solution time, and preprocessing time) of the method

proposed in this paper is significantly lower than that of the other two methods. This is because although traditional finite element methods are highly accurate and particularly suitable for stress–strain analysis of continuous media, the computational complexity increases sharply with mesh density (n). The voxel model method is simple to model, but it increases computational complexity during the detailed calculation stage. The voxel octree model method proposed in this paper achieves a balance between accuracy and efficiency by performing local refinement in the cutting area and thin-walled critical locations, and using coarse voxels in areas far from the cutting area.

Table 4. Simulation time for deformation prediction.

Method	Time
The traditional FEM	2.4 h
The voxel model method	965 s
The voxel octree model method	837 s

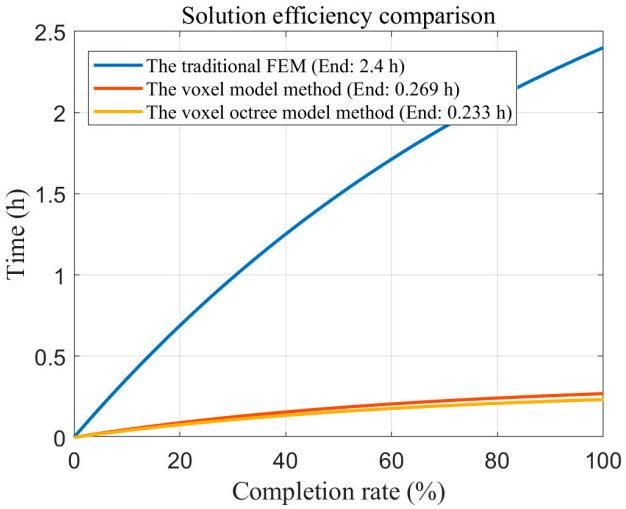


Figure 19. Comparison of the computational efficiency of the three methods.

Table 5. Computational Performance Comparison.

Method	The Voxel Octree Model Method	The Voxel Model Method	The Traditional FEM
Time complexity	$O\ (n{\cdot}logn)$	$O((n_c + n_f){\cdot}n_f^{1/3})$	$O\ (n^{4/3})$
Memory occupancy (MB)	320	368	2413
Single step solution time (um)	89	101	803
Preconditioning time (s)	2.8	1.9	43.2

Finally, the Introduction notes that milling thin-walled workpieces often involves dynamic instability, particularly regenerative chatter. This phenomenon arises from the coupling between tool vibration and the periodically varying chip thickness. The voxel octree model method proposed in this paper introduces a strategy for removing and updating the stiffness matrix, enabling accurate predictions for the thin-walled workpiece deformation under quasi-static modeling conditions. This work lays the research foundations for subsequent dynamic analysis.

5. Conclusions

This paper proposes a voxel octree method for efficiently predicting flank milling deformation of thin-walled workpieces. First, a micro-element milling force prediction model is established based on the equivalent shear force model. Then, through tool-workpiece

collision detection analysis, a construction strategy for the voxel octree model is proposed. For thin-walled workpieces, voxel unit adaptive division is performed from coarse to fine, and a corresponding voxel unit stiffness matrix is established. Finally, the workpiece deformation is accurately calculated through the milling force model and stiffness matrix. The experimental results show that the proposed method is highly consistent with the actual measured value in predicting the deformation of thin-walled workpieces. At the same time, compared with the traditional FEM and the voxel model method, the calculation time is significantly reduced, and the efficiency is improved by 90% and 13.2%, respectively. This method provides an effective solution for the rapid prediction of workpiece deformation and can significantly improve the efficiency of process preliminary research.

This paper mainly focuses on the prediction of flank milling deformation of thin-walled workpieces with a fixed tool axis. In future work, this method will be further used to predict the thin-walled workpiece deformation under five-axis machining with a variable tool axis. At the same time, the influence of tool deformation on the thin-walled workpiece deformation during machining will be further considered. Finally, since some scholars have pointed out certain shortcomings in Altintas' milling force model, subsequent studies will use this model dialectically and further investigate a more accurate milling force model.

Author Contributions: Methodology, investigation, software, and writing—original draft: P.W.; Project administration and funding acquisition: W.L.; Investigation, review and editing: L.W. All authors have read and agreed to the published version of the manuscript.

Funding: This research was supported by the National Natural Science Foundation of China (Nos. 52375448, 52305480).

Data Availability Statement: Data and materials used in this research are available.

Acknowledgments: We sincerely acknowledge the invaluable guidance and support provided by Guang Yu during the revision of this manuscript.

Conflicts of Interest: The authors confirm that the research was conducted in the absence of any commercial or financial relationships that could be construed as a potential conflict of interest.

References

1. Radu, P.; Schnakovszky, C. A Review of Proposed Models for Cutting Force Prediction in Milling Parts with Low Rigidity. *Machines* **2024**, *12*, 140. [CrossRef]
2. Zhou, J.; Qi, Q.; Liu, Q.; Wang, J.; Jiang, X.; Feng, P. Determining residual stress profile induced by end milling from measured thin plate deformation. *Thin-Walled Struct.* **2024**, *200*, 111862. [CrossRef]
3. Wang, L.; Li, W.; Yu, G. Optimal deformation error compensation process in flank milling of thin-walled work-pieces. *Int. J. Adv. Manuf. Technol.* **2023**, *126*, 4353–4367. [CrossRef]
4. Ge, G.; Xiao, Y.; Feng, X.; Li, B.; Wang, T.; Zhang, J. An efficient prediction method for the dynamic deformation of thin-walled parts in flank milling. *Comput. Aided Des.* **2022**, *152*, 103401. [CrossRef]
5. Yang, C.; Yu, R.; Jiang, S. A cyclic calibration method of milling force coefficients considering elastic tool deformation. *Machines* **2023**, *11*, 821–834. [CrossRef]
6. Li, Z.; Yan, Q.; Tang, K. Multi-pass adaptive tool path generation for flank milling of thin-walled workpieces based on the deflection constraints. *J. Manuf. Process.* **2021**, *68*, 690–705. [CrossRef]
7. Liu, H.; Wang, C.; Zeng, L.; Zhang, X.; Chen, Y. Prediction of icing interface normal stress response for thin-walled parts machining with ice-based fixturing (IBF). *Thin-Walled Struct.* **2023**, *188*, 110807. [CrossRef]
8. Tang, J.; Deng, C.; Chen, X.; Zhai, H. Analysis and optimization of milling deformations of TC4 alloy thin-walled parts based on finite element simulations. *Machines* **2023**, *11*, 628–642. [CrossRef]
9. Yan, Q.; Luo, M.; Tang, K. Multi-axis variable depth-of-cut machining of thin-walled workpieces based on the workpiece deflection constraint. *Comput. Aided Des.* **2018**, *100*, 14–29. [CrossRef]
10. Landwehr, M.; Schmid, S.; Holla, V.; Kirsch, B.; Aurich, J.C. The finite cell method for the prediction of machining distortion caused by initial residual stresses in milling. *Procedia CIRP* **2021**, *102*, 144–149. [CrossRef]

11. Peng, Z.; Zhou, H.; Li, G.; Zhang, X.; Wang, J.; Chen, Y. A detected-data-enhanced FEM for residual stress reconstruction and machining deformation prediction. *Alex. Eng. J.* **2024**, *91*, 334–347. [CrossRef]
12. Zhang, Z.; Luo, M.; Tang, K.; Wang, X.; Chen, Y.; Li, H. A new in-process active control method for reducing the residual stresses induced deformation of thin-walled parts. *J. Manuf. Process.* **2020**, *59*, 316–325. [CrossRef]
13. Choi, H.; Choi, S.; Kang, S.C.; Lee, J.H.; Park, S.H.; Kim, J.B. Prediction of anisotropic strengths of steel plate after prior bending-reverse bending deformation: Application of distortional hardening model. *Int. J. Mech. Sci.* **2021**, *204*, 106512. [CrossRef]
14. Wang, Z.; Sun, J.; Liu, L.; Chen, X.; Zhang, Y.; Li, R. An analytical model to predict the machining deformation of frame parts caused by residual stress. *J. Mater. Process. Technol.* **2019**, *274*, 116282. [CrossRef]
15. Nishida, I.; Okumura, R.; Sato, R.; Kono, D.; Fujishima, M. Cutting force simulation in minute time resolution for ball end milling under various tool posture. *J. Manuf. Sci. Eng.* **2018**, *140*, 021009. [CrossRef]
16. Kaneko, K.; Shimizu, J.; Shirase, K. A voxel-based end milling simulation method to analyze the elastic deformation of a workpiece. *J. Manuf. Sci. Eng.* **2023**, *145*, 011005. [CrossRef]
17. Wang, J.; Quan, L.; Tang, K. A prediction method based on the voxel model and the finite cell method for cutting force-induced deformation in the five-axis milling process. *Comput. Methods Appl. Mech. Eng.* **2020**, *367*, 113110. [CrossRef]
18. Jose, D.; Daniel, O.; Gorka, U.; Oscar, M.; Alex, E.; Luis, N. Uncharted Stable Peninsula for Multivariable Milling Tools by High-Order Homotopy Perturbation. *Method. Appl. Sci.* **2020**, *10*, 7869–7891.
19. Sol, I.; Rivero, A.; Lacalle, L.; Gamez, A. Thin-Wall Machining of Light Alloys: A Review of Models and Industrial Approaches. *Materials* **2019**, *12*, 2012–2040. [CrossRef]
20. Li, W.; Wang, L.; Yu, G. Chatter prediction in flank milling of thin-walled parts considering force-induced deformation. *Mech. Syst. Signal Process.* **2022**, *165*, 108314. [CrossRef]
21. Altintas, Y. *Manufacturing Automation: Metal Cutting Mechanics, Machine Tool Vibrations, and CNC Design*, 2nd ed.; Cambridge University Press: Cambridge, UK, 2012; pp. 4–65.
22. Astakhov, V. Cutting Force Modeling: Genesis, State of the Art, and Development. In *Mechanical and Industrial Engineering*; Davim, J., Ed.; Springer Nature: Berlin, Germany, 2022; pp. 39–93.
23. Wang, L.; Si, H.; Guan, L.; Liu, Z. Comparison of different polynomial functions for predicting cutting coefficients in the milling process. *Int. J. Adv. Manuf. Technol.* **2018**, *94*, 2961–2972. [CrossRef]
24. Armin, H.; Wurm, K.; Bennewitz, M.; Stachniss, C.; Burgard, W. OctoMap: An efficient probabilistic 3D mapping framework based on octrees. *Auton. Robot.* **2013**, *34*, 189–206. [CrossRef]
25. Cappellini, C.; Abeni, A. An analytical micro-milling force model based on the specific cutting pressure-feed dependence, in presence of ploughing and tool run-out effects. *J. Manuf. Process.* **2024**, *116*, 224–245. [CrossRef]
26. Aslantas, K.; Ülker, S.; Şahan, Ö.; Pimenov, D.; Giasin, K. Mechanistic modeling of cutting forces in high-speed microturning of titanium alloy with consideration of nose radius. *Int. J. Adv. Manuf. Technol.* **2022**, *119*, 2393–2408. [CrossRef]
27. Attanasio, A. Tool Run-Out Measurement in Micro Milling. *Micromachines* **2017**, *8*, 221–237. [CrossRef] [PubMed]

Disclaimer/Publisher's Note: The statements, opinions and data contained in all publications are solely those of the individual author(s) and contributor(s) and not of MDPI and/or the editor(s). MDPI and/or the editor(s) disclaim responsibility for any injury to people or property resulting from any ideas, methods, instructions or products referred to in the content.